Martirosyan, N., Efthimiopoulos, I., Pennacchioni, L., Wirth, R., Jahn, S., Koch-Müller, M. (2021): Effect of cationic substitution on the pressure-induced phase transitions in calcium carbonate. - American Mineralogist, 106, 549-558.

https://doi.org/10.2138/am-2021-7547

American Mineralogist, Volume 106, pages 549–558, 2021

Effect of cationic substitution on the pressure-induced phase transitions in calcium carbonate

Naira S. Martirosyan[1,2,*], Ilias Efthimiopoulos[1], Lea Pennacchioni[1,3], Richard Wirth[1], Sandro Jahn[2], and Monika Koch-Müller[1]

[1]GFZ German Research Centre for Geosciences, Telegrafenberg, 14473 Potsdam, Germany
[2]Institute of Geology and Mineralogy, University of Cologne, Zülpicher Str. 49b, 50674 Cologne, Germany
[3]Institute of Geosciences, Goethe University, Altenhöferallee 1, 60438 Frankfurt am Main, Germany

Abstract

The high-pressure $CaCO_3$ phase diagram has been the most extensively studied within the carbon-ates group. However, both the diverse mineralogy of carbonates and the abundance of solid solutions in natural samples require the investigation of multi-component systems at high pressures (*P*) and temperatures (*T*). Here we studied a member of the $CaCO_3$–$SrCO_3$ solid-solution series and revealed the effect of cationic substitution on the pressure-induced phase transitions in calcium carbonate.

A synthetic solid solution $Ca_{0.82}Sr_{0.18}CO_3$ was studied in situ by Raman spectroscopy in a diamond-anvil cell (DAC) up to 55 GPa and 800 K. The results of this work show significant differences in the high-pressure structural and vibrational behavior of the $(Ca,Sr)CO_3$ solid solution compared to that of pure $CaCO_3$. The monoclinic $CaCO_3$-II-type structure (Sr-calcite-II) was observed already at ambient conditions instead of the "expected" rhombohedral calcite. The stress-induced phase transition to a new high-pressure modification, termed here as Sr-calcite-IIIc, was detected at 7 GPa. Sr-calcite-VII formed already at 16 GPa and room *T*, which is 14 GPa lower compared to $CaCO_3$-VII. Finally, crys-tallization of Sr-aragonite was detected at 540 K and 9 GPa, at 200 K lower *T* than pure aragonite. Our results indicate that substitution of Ca^{2+} by bigger cations, such as Sr^{2+}, in $CaCO_3$ structures can stabilize phases with larger cation coordination sites (e.g., aragonite, $CaCO_3$-VII, and post-aragonite) at lower *P-T* conditions compared to pure $CaCO_3$. The present study shows that the role of cationic composition in the phase behavior of carbonates at high pressures should be carefully considered when modeling the deep carbon cycle and mantle processes involving carbonates, such as metasomatism, deep mantle melting, and diamond formation.

Keywords: Deep carbon cycle, calcium carbonate, solid solution, phase diagram, phase transition, high pressure, vibrational spectroscopy

Introduction

Investigations of natural samples such as mantle xenoliths, carbonatites and kimberlites, inclusions in diamonds, and car-bonate-bearing rocks from the ultrahigh-pressure metamorphic terranes provide direct evidence of the existence of carbonates and carbonatite melts in the Earth's deep upper mantle, transi-tion zone, and lower mantle (Stachel et al. 2000; Brenker et al. 2007; Logvinova et al. 2008, 2011, 2019a, 2019b; Kaminsky et al. 2009, 2013; Korsakov et al. 2009; Kamenetsky and Yaxley 2015; Sharygin et al. 2015). Syngenetic inclusions in diamonds and other mantle minerals frequently contain calcium carbonates, dolomite, magnesite, and ankerite (Stachel et al. 2000; Brenker et al. 2007; Logvinova et al. 2008, 2011, 2019a, 2019b; Kaminsky et al. 2009, 2013; Korsakov et al. 2010). The abundance of the calcium carbonate at near surface and mantle conditions, and its overall geological significance have triggered an enormous interest in the $CaCO_3$ phase diagram (Suito et al. 2001; Ono et al. 2005, 2007; Merlini et al. 2012, 2018; Pippinger et al. 2014; Koch-Müller et al. 2016; Gavryushkin et al. 2017; Lobanov et al. 2017; Bayarjargal et al. 2018).

At atmospheric pressure, $CaCO_3$ crystallizes predominantly in the rhombohedral calcite structure [space group *R3c*] with coplanar CO_3^{2-} groups and Ca^{2+} in sixfold coordination ($Ca^{[6]}$). Compression of calcite leads to a complex polymorphism with several phase transitions. Previous experimental and computa-tional studies revealed four stable high-pressure polymorphs of calcite: aragonite (*Pnma*, $Ca^{[9]}$), $CaCO_3$-VII ($P2_1/c$, $Ca^{[10]}$), post-aragonite (*Pmmn*, $Ca^{[12]}$), and sp^3-$CaCO_3$ ($P2_1/c$, $Ca^{[12]}$, $C^{[4]}$) (Fig. 1) (Ono et al. 2005, 2007; Gavryushkin et al. 2017; Lobanov et al. 2017; Bayarjargal et al. 2018). The formation of these high-pressure phases is kinetically hindered at ambient temperature and occurs only above 773 K (500 °C) (Bayarjargal et al. 2018). Cold compression of calcite, on the contrary, leads to a dif-ferent sequence of high-pressure polymorphs: $CaCO_3$-II ($P2_1/c$, $Ca^{[6]}$); $CaCO_3$-III and -IIIb ($P1$, $Ca^{[7]}$ and $Ca^{[9]}$); $CaCO_3$-VI ($P1$, $Ca^{[7+2]}$) (Fig. 1) (Suito et al. 2001; Merlini et al. 2012, 2018; Koch-Müller et al. 2016; Bayarjargal et al. 2018). All of these high-pressure modifications are considered metastable (Suito et al. 2001; Merlini et al. 2012, 2018; Koch-Müller et al. 2016; Bayarjargal et al. 2018). Such consideration arises from the fact that those polymorphs appear within the stability fields of

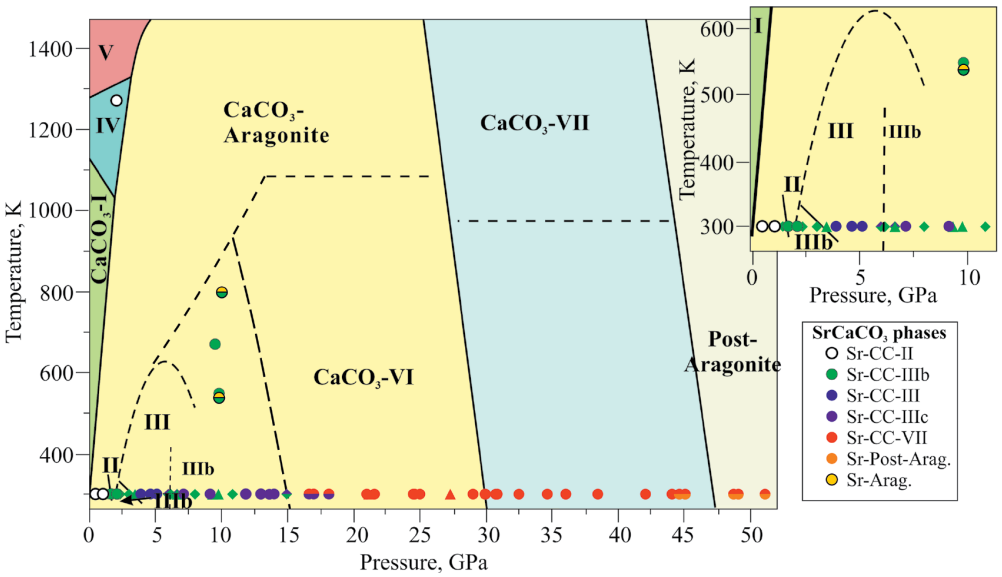

Figure 1. Experimental conditions and phase identification of $(Ca,Sr)CO_3$ solid solution in comparison with $CaCO_3$ phase diagram. Symbols show the *P-T* conditions of the present study. For more details on the room-temperature experiments see inset and Online Materials[1] Figure OM1. Detected polymorphs are marked with different colors (also shown in the legend). Seven high-*P* phases of $(Ca,Sr)CO_3$ were detected: Sr-calcite-II (Sr-CC-II); Sr-calcite-IIIb (Sr-CC-IIIb); Sr-calcite-III (Sr-CC-III); Sr-calcite-IIIc (Sr-CC-IIIc); Sr-calcite-VII (Sr-CC-VII); Sr-aragonite (Sr-Arag); and Sr-post-aragonite (Sr-Post-Arag). Black text and lines represent the known phase diagram of $CaCO_3$ (Irving and Wyllie 1973; Suito et al. 2001; Ono et al. 2005; Ter Heege and Renner 2007; Pippinger et al. 2014; Koch-M¿ller et al. 2016; Gavryushkin et al. 2017; Bayarjargal et al. 2018). (Color online.)

aragonite and $CaCO_3$-VII, yet density functional theory (DFT) calculations predict that they have higher enthalpies at 0 K and lower densities than aragonite and $CaCO_3$-VII (Koch-M¿ller et al. 2016; Gavryushkin et al. 2017; Bayarjargal et al. 2018).

The $CaCO_3$ system is well studied both at near surface condi-tions and at high pressures (Fig. 1). However, the

mineralogy of carbonates is more diverse, and natural calcium carbonates are often found as solid solutions with Mg^{2+}, Fe^{2+},Sr^{2+}, Ba^{2+}, Na^{+}, and K^{+}. The calcium carbonate solid solutions are widely used in geochemistry, paleoceanographic reconstructions, and isotope chemostratigraphy (Kuznetsov et al. 2014).

The diversity of carbonate compositions found in diamond inclusions and in other mantle minerals reflects the rich mantle mineralogy of carbonates. Besides (Ca,Mg,Fe)-carbonates, they may contain nyerereite $[Na_2Ca(CO_3)_2]$ (Kaminsky et al. 2009), b¿tschliite $[K_2Ca(CO_3)_2]$ (Logvinova et al. 2019b), and other sodium- and potassium-bearing carbonates, as well as a variety of $(Ba,Ca)CO_3$, $(Sr,Ca)CO_3$, and $(Ca,Ba,Sr)CO_3$ (Logvinova et al. 2008, 2011, 2019a; Kaminsky et al. 2009). Concentrations of Ba^{2+} and Sr^{2+} in natural calcium carbonate inclusions in diamonds and other mantle minerals can vary from a few hundredths of mole percent (0.06ð0.7 mol%) (Kaminsky et al. 2009; Korsakov et al. 2010) to highly enriched varieties (5ð18 mol%) (Klein-BenDavid et al. 2006, 2009; Logvinova et al. 2008, 2011, 2019a). It has been proposed that the high concentration of Ba^{2+} and Sr^{2+} could be a strong indication of deep metasomatic processes (Logvinova et al. 2008, 2011, 2019a).

Given the significant role of carbonates in mantle processes, such as partial melting of peridotites and Hirschmann 2006; Kiseeva et al. 2013), metasomatism (Yaxley et al. 1991; Kiseeva et al. 2012) and diamond formation (Paly-anov et al. 1999; Stachel and Harris 2008), and the diversity of compositions found in natural samples, studies of phase diagrams at different *P-T* conditions in the multi-component carbonate systems are of great importance.

The solid solution systems $CaCO_3$-$SrCO_3$ and $CaCO_3$-$BaCO_3$ are poorly studied at high pressures. Unlike $CaCO_3$, the end-members $SrCO_3$ and $BaCO_3$ have simple phase diagrams. They crystallize in the orthorhombic aragonite structure up to 22 GPa ($SrCO_3$) and 10 GPa ($BaCO_3$) and transform to post-aragonite with further pressure increase (Wang et al. 2015; Biedermann et al. 2020). The binary $CaCO_3$-$SrCO_3$ system has been studied at *P-T* conditions up to 1.6 GPa and 923 K (650 ÁC) (Carlson 1980). It was demonstrated that small amounts of Sr^{2+} expand the stability region of the aragonite phase.

To better understand the role played by the Sr^{2+} substitution on the complex polymorphism of calcium carbonate at mantle pressures and temperatures, more experimental work has to be performed on the $CaCO_3$-$SrCO_3$ system at extreme conditions. In this study, we synthesized a $(Ca,Sr)CO_3$ solid solution at 2 GPa and 1273 K and conducted in situ high-pressure and temperature experiments up to 55 GPa and 800 K in diamond-anvil cells using Raman spectroscopy.

Experimental methods

Sample synthesis and characterization

$(Ca,Sr)CO_3$ solid solution was synthesized at 2 GPa and 1273 K (1000 ÁC) (Fig. 1) in a Walker type multi-anvil apparatus at GFZ Potsdam (Walker et al. 1990). The run

duration was 8 h. The starting material was prepared from analytical-grade synthetic powders of $CaCO_3$ and $SrCO_3$ (99.999% purity, Sigma Aldrich Chemical Company), with 20 mol% $SrCO_3$ in the initial mixture. The blended mixture was placed into a Pt capsule. A Cr-doped MgO octahedron with an edge length of 18 mm and other MgO-based parts were used as pressure transmitting media. Heat was generated with a stepped graphite heater. Temperature was controlled using a $W_{5\%}Re$-$W_{26\%}Re$ type C thermocouple. Eight tungsten carbide cubes with the truncation edge length of 11 mm were used as Kawai-type anvils. The sample was analyzed by electron microprobe (EMP), transmission electron microscopy (TEM), powder X-ray diffraction (XRD), Fourier transform infrared (FTIR), and Raman spectroscopy.

The chemical composition of the synthesized sample (Online Materials[1] Table OM1 and Fig. OM2) was determined with EMP analyses using a JEOL Hyperprobe JXA-8500F EMP with a field emission cathode (GFZ, Potsdam). Analysis was conducted at a 15 kV acceleration voltage, a 10 nA beam current, and a 0.5–10 µm beam size. Dolomite and strontianite were used as standards.

TEM with a high-resolution energy-dispersive spectrometer was used for the microtexture observation and preliminary structural analysis (Fig. 2; Online Materials[1] Fig. OM3). Thin sections of approximately 15 × 10 × 0.15 μm^3 size were prepared with a focused Ga-ion beam (FIB) system (FEI FIB 200 TEM) (Wirth 2009) directly from the crystals in the microprobe mounts, and analyzed using a FEI Tecnai G2 F20

X-Twin transmission electron microscope (GFZ, Potsdam).

The structural analysis was performed with XRD. The XRD patterns were measured at atmospheric pressure using a STOE Stadi P diffractometer equipped with a curved Germanium (111) primary monochromator, a high-resolution MYTHEN-detector and a normal focus Cu X-ray tube ($CuK\alpha_1$ radiation) (GFZ, Potsdam). The XRD data were processed with the GSAS II software package (Toby and Von Dreele 2013). Unit-cell parameters were obtained by Le Bail/Pawley refinements (Fig. 3).

FTIR measurements in the mid-infrared region were conducted with the Ver-tex 80v FTIR spectrometer combined with a Hyperion 2000 microscope (GFZ, Potsdam) within a 500–2000 cm^{-1} spectral range (Fig. 4; Online Materials[1] Fig. OM4). We used a KBr beamsplitter and a mercury-cadmium-telluride detector. The spectra were averaged over 1536 scans with a spectral resolution of 2 cm^{-1}. The description of the Raman measurements is given in the section below.

High pressure in situ experiments

Pressure-induced phase transitions in the $Ca_{0.82}Sr_{0.18}CO_3$ solid solution were studied in situ using Raman spectroscopy at room and at high temperatures up to 800 K (Fig. 1; Online Materials[1] Fig. OM1). Two different types of diamond-anvil cells (DACs) were employed, depending on the target temperature.

Symmetric piston-cylinder DACs with 250 µm culet size diamonds were used for the room-temperature experiments. Rhenium gaskets were indented to a thickness of 30–40 µm and drilled in the center of the indentation to form a sample chamber. The crystals were carefully selected, cleaned with ethanol, and placed into the sample chamber together with ruby spheres acting as pressure sensors. Liquid argon (Ar) was loaded cryogenically as a pressure-transmitting medium, follow-ing the same procedure as in Koch-Müller et al. (2016). Pressure was measured using laser-induced fluorescence spectroscopy of ruby (Al_2O_3:Cr^{3+}) (Dewaele et al. 2008). Previous studies have shown that the ruby scale is accurate within 2–5% up to 55 GPa (Dewaele et al. 2008). Four different experimental high-pressure runs were conducted at room temperature (Fig. 1; Online Materials[1] Fig. OM1). Raman spectra were measured in 1–2 GPa steps up to 55 GPa, both on compression and decompression cycles (Online Materials[1] Fig. OM1).

The second set of experiments was performed using an internally heated membrane-driven DAC (DAC-HT) [Diacell µScopeDAC HT (G), EasyLab, U.K.], equipped with diamonds of 300 µm culet size. The measurements were carried out in the 9–10 GPa pressure range and at high temperatures from 540 to 800 K (Fig. 1). The sample, together with SrB_4O_7:Sm^{2+} powder and ruby spheres used as *P-T* sensors, was sandwiched between two NaCl layers and placed inside the sample chamber. NaCl served both as a pressure medium and as a thermal insula-tor. The temperature in the DAC-HT experiments was measured both outside the sample chamber with a K-type thermocouple placed close to the lower diamond, as well as inside the sample chamber using the fluorescence lines of SrB_4O_7:Sm^{2+} and ruby (Datchi et al. 2007). Details of the temperature calibrations are given in Online materials. The *P-T* calibration method allows to determine pressure with a 0.4–1.2% and temperature with a 1.0–1.3% accuracy up to 20 GPa and 900 K (Datchi et al. 2007; Romanenko et al. 2018). The temperature outside the gasket hole, measured by the thermocouple, was always lower than that estimated inside the sample chamber, with the difference reaching about 50 K at the maximum temperature of 800 K.

The Raman spectra in both room and high-*T* experiments were measured with a HORIBA Jobin Yvon LabRAM HR800 VIS spectrometer (GFZ, Potsdam) equipped with a blue 473 nm diode-pumped solid-state laser. The spectral range for the measurements was 140–1200 cm^{-1} and the data acquisition time was 120 s. The spectra were collected at ambient conditions before and after the pressure increase and at high pressures both upon compression and decompression (Online Materials[1] Fig. OM1). The measurements at high temperature were performed every 2–5 min. The software Fityk (Wojdyr 2010) was used for data analysis.

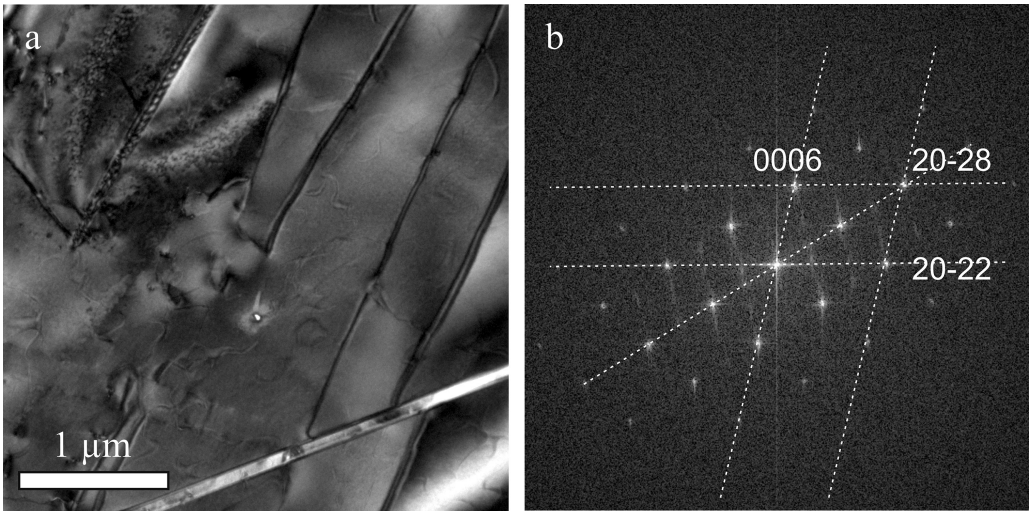

Figure 2. Results of the TEM analysis performed on the $Ca_{0.82}Sr_{0.18}CO_3$ solid solution: (**a**) the lamellar texture of the sample, (**b**) the electron diffraction pattern. The lines in **b** represent the unit cell of calcite with *R3c* space group with *a* = 5.01 Å and *c* = 17.25 Å. The EDX spectra are given in Online Materials[1] Figure OM3.

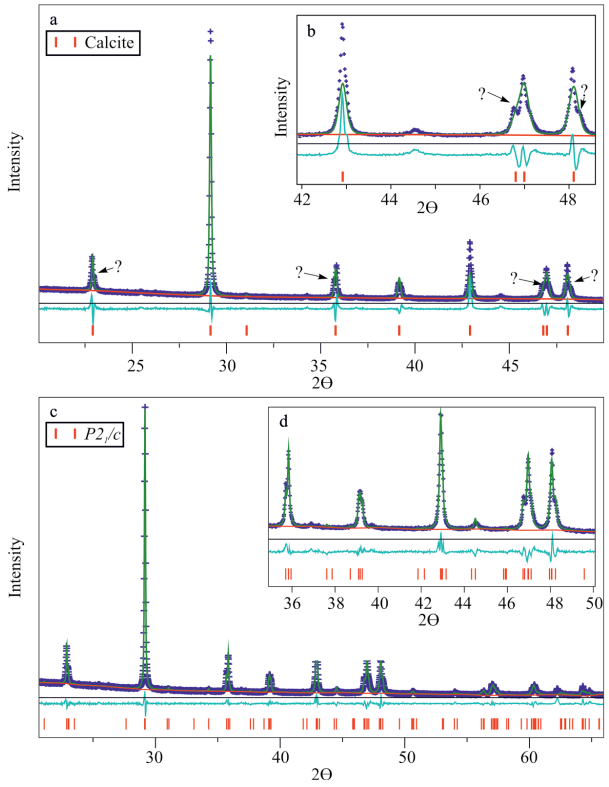

Figure 3. The results of the Pawley refinement for the $Ca_{0.82}Sr_{0.18}CO_3$ solid solution (Sr-calcite-II) using (**a** and **b**) calcite (*R*3*c*) and (**c** and **d**) $CaCO_3$-II ($P2_1/c$) as a model. The XRD patterns were obtained at ambient conditions. Insets on top (**b** and **c**) show magnified region with splitted peaks. The calculated Bragg reflection positions of $CaCO_3$-II and calcite are marked with red vertical bars; experimental patterns = dark blue crosses, calculated patterns = green line; difference profiles = blue line; and background profiles = red line. (Color online.)

Experimental results

Characterization of the synthesized (Ca,Sr)CO_3 solid solution

Backscattered electron images of the synthesized samples are presented in Online Materials[1] Figure OM2. The recovered sample consists of large (≥30–100 μm) grains of (Ca,Sr)CO_3 solid solution with homogeneous composition and Sr^{2+} content of 18 mol% according to the EMP analyses (Online Materials[1] Table OM1). Some of the grains contain small inclusions ≤1–2 μm in size, located primarily in voids and cracks (Online Materials[1] Fig. OM2b).

Two thin films from different grains were prepared for the TEM analysis by the focused ion beam method (Fig. 2; Online Materials[1] Fig. OM3). The samples have a high density of dislocations

and a lamellar texture with clear interfaces caused by complex twining (Fig. 2a). Analytical TEM confirmed that both samples have homogeneous compositions and consist predominantly of crystalline Ca-rich (Ca~80 mol%) (Ca,Sr)CO_3 solid solution (Online Materials[1] Figs. OM3a and OM3c). The electron diffraction pattern of the main phase was refined in the rhombohedral calcite unit cell; however, we see several additional low-intensity reflections (Fig. 2b). The few grains of the secondary Sr-rich (Sr, Ca)CO_3 phase, which constitutes less than 1 vol% of the thin film, were detected as small inclusions along the dislocations and cracks (Online Materials[1] Figs. OM3a and OM3b). The electron diffraction pattern of the secondary phase could be refined with orthorhombic symmetry.

Most of the reflections in the XRD pattern of the $Ca_{0.82}Sr_{0.18}CO_3$ solid solution, including the one with the highest intensity, can be refined in the calcite structure (Figs. 3a and 3b) with lattice parameters a = 5.01 Å, c = 17.25 Å (residual factor wR_p = 19%). However, several low-intensity peaks located at 2θ = 23, 36, 47, and 48° show a splitting incompatible with the calcite structure (Figs. 3a and 3b). The attempts to include an orthorhombic phase, as observed in the TEM analyses, did not improve the XRD refinement. It is likely that due to the low concentration, the secondary phase does not appear in the XRD pattern. The best fit for all of the observed Bragg peaks was achieved using a monoclinic unit cell similar to that of $CaCO_3$-II (wR_p = 8.3%, Figs. 3c and 3d) (Merrill and Bassett 1975). The refined unit cell of $Ca_{0.82}Sr_{0.18}CO_3$ solid solution has $P2_1/c$ space group with the following lattice parameters: a = 6.44 Å; b = 5.02 Å; c = 8.13 Å; β = 108.13°. For comparison, the lattice parameters of pure $CaCO_3$-II are a = 6.33 Å; b = 4.95 Å; c = 8.03 Å; β = 107.9° at 1.5 GPa (Merrill and Bassett 1975).

The difference in the structure of the synthesized solid solution from that of calcite was also indicated by the results of the mid-infrared (MIR) and Raman measurements (Figs. 4 and 5; Online Materials[1] Fig. OM4–OM6). The vibrational spectrum of calcite contains 4 fundamental internal modes, assigned to CO_3^{2-} vibrations: symmetric stretching (v_1), out-of-plane bending (v_2), asymmetric stretching (v_3), and in-plane bending (v_4) (White 1974) (Fig. 4; Online Materials[1] Fig. OM5). The v_1 and v_2 modes are Raman- (v_1) or infrared- (v_2) active only, while the v_3 and v_4 bands can be detected in both Raman and IR spectra (White 1974).

The fundamental modes in the MIR-spectrum of pristine $CaCO_3$ calcite are located at 872 cm^{-1} (v_2), 1407 cm^{-1} (v_3), and 712 cm^{-1} (v_4) (Fig. 4) (White 1974; Vahur et al. 2016). Addi-tionally, spectra can exhibit a satellite mode at 1660 cm^{-1} and a combination band at 1750 cm^{-1} (v_1+v_4). The MIR spectrum of the studied $Ca_{0.82}Sr_{0.18}CO_3$ solid solution differs from that of calcite, as both of the v_2 and v_4 bending modes split into doublets separated by ~10 cm^{-1}, and additional modes appear at 1085 cm^{-1} (v_1), 859 cm^{-1}, and at 1740 cm^{-1} (Fig. 4; Online Materials[1] Fig. OM4). The appearance of these new modes, in particular the IR-forbidden v_1 band and the apparent splitting of the bending modes, clearly indicate a lower crystalline symmetry of the solid solution compared to pure calcite, at least on the local scale (White 1974). Similar IR features were previously observed in the infrared spectra of $CaCO_3$-II, collected in situ at 1.9 GPa (Koch-Müller et al. 2016), and in barytocalcite $CaBa(CO_3)_2$ ($P2_1/m$) (Scheetz and White 1977). Both of these phases have structures derivative of calcite.

Raman spectra of $Ca_{0.82}Sr_{0.18}CO_3$ were collected at atmo-spheric pressure in the range of 100–1250 cm^{-1} (Fig. 5; Online Materials[1] Figs. OM5–OM6). The following modes are assigned to internal vibrations of the $(CO_3)^{2-}$ group: 1087 cm^{-1} with a sat-ellite mode at 1066 cm^{-1} (v_1), 711 cm^{-1} with a shoulder band at

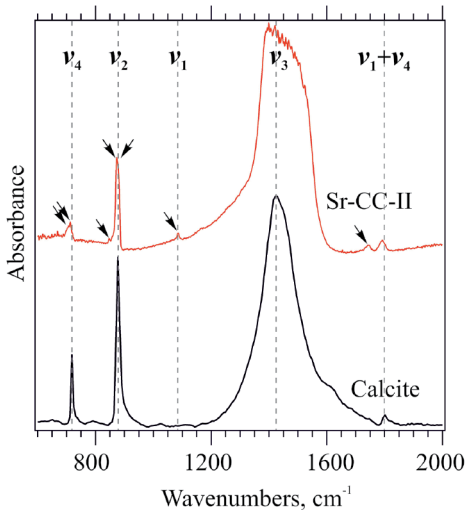

Figure 4. Mid IR spectrum of the $Ca_{0.82}Sr_{0.18}CO_3$,Sr-calcite-II (Sr-CC-II), in comparison with spectrum of $CaCO_3$ calcite [from IR database (Vahur et al. 2016)]. The spectrum of calcite contains 4 modes (shown by gray dashed lines): 712 cm^{-1} (v_4); 872 cm^{-1} (v_2); 1407 cm^{-1} (v_3); and 1750 cm^{-1} (v_1+v_4). In the MIR spectrum of the Sr-CC-II the v_2 and v_4 bending modes are splitted, additional modes appear at 1085 cm^{-1} (v_1), 859 cm^{-1}, and at 1740 cm^{-1} (all marked by arrows). The fitting of the bands of the $Ca_{0.82}Sr_{0.18}CO_3$ spectrum is illustrated in Online Materials[1] Figure OM4. (Color online.)

706 cm^{-1} (v_4), and a third peak at 875 cm^{-1} (v_2) (Online Materials[1] Figs. OM6 and OM7). Three main low-frequency bands located at 148, 190, and 275 cm^{-1} correspond to lattice vibrations (Online Materials[1] Fig. OM6). All bands, with the exception of the 706, 190, and 875 cm^{-1} can be assigned to calcite, yet shifted to lower wavenumbers due to the expansion of the unit cell caused by the presence of the larger Sr^{2+} cations (Online Materials[1] Fig. OM5). The low-intensity mode at 875 cm^{-1} (Online Materials[1]

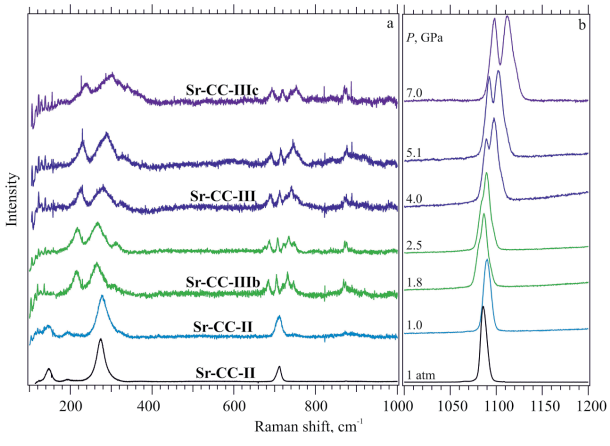

Figure 5. Raman spectra of $Ca_{0.82}Sr_{0.18}CO_3$ solid solution collected upon compression up to 7 GPa. Four high-P phases were observed: Sr-calcite-II (Sr-CC-II), Sr-calcite-IIIb (Sr-CC-IIIb), Sr-calcite-III (Sr-CC-III), and Sr-calcite-IIIc (Sr-CC-IIIc). Raman spectrum collected before the experiment is shown in black. For more details see run 3 in Online Materials[1] Figure OM1. (Color online.)

Fig. OM6) corresponds to the out-of-plane bending vibration (v_2), a Raman-inactive vibration in the calcite structure (White 1974). As in the MIR case, the observation of additional modes indicates a lower symmetry of $Ca_{0.82}Sr_{0.18}CO_3$ compared to that of rhombohedral calcite.

Previously proposed as a main feature of the $CaCO_3$-II polymorph (Pippinger et al. 2014) was the appearance of the additional lattice vibration mode at 190 cm^{-1} and the clear splitting of the v_4 band in the Raman spectra. It should be noted, however, that while 190 cm^{-1} could be unequivocally distinguished in the spectra of $Ca_{0.82}Sr_{0.18}CO_3$, the splitting of v_4 band is not appar-ent, and the "extra" component appears as a shoulder (Online Materials[1] Fig. OM6). Possible reasons behind the absence of a clear v_4 band splitting might be the spectral resolution, as well as the structural differences between $Ca_{0.82}Sr_{0.18}CO_3$ and $CaCO_3$-II at a microstructural scale.

Overall, all of our collected data allow us to conclude that the structure of the synthesized $Ca_{0.82}Sr_{0.18}CO_3$ phase at ambient conditions has a lot of similarities with that of $CaCO_3$-II and can be viewed as a monoclinic distortion of the rhombohedral calcite structure. Therefore, we will call this new phase Sr-calcite-II.

High-pressure Raman study

The results of the in situ high-pressure study of the $Ca_{0.82}Sr_{0.18}CO_3$ solid solution are summarized in Figures 5–7 and in Online Materials[1] Figs. OM7–OM13. Since the Raman spectra of the detected high-pressure polymorphs are similar to those of $CaCO_3$ high-pressure modifications, the same nomenclature is used. The Raman spectra collected in the compression experiments at room temperature are shown in Figures 5 and 6. The first phase transition was detected at 1.8 GPa. New bands appear at 1080 cm^{-1} (Fig. 5; Online Materials[1] Fig. OM7) and below 900 cm^{-1}, where we observe at least 10 new bands (Fig. 5; Online Materials[1] Fig. OM9). The arising features of the Raman spectra are in good agreement with previous studies on the pure $CaCO_3$ system (Pippinger et al. 2014; Koch-Müller et al. 2016), resembling the $CaCO_3$-IIIb Raman pattern. Thus, the $Ca_{0.82}Sr_{0.18}CO_3$ solid solu-

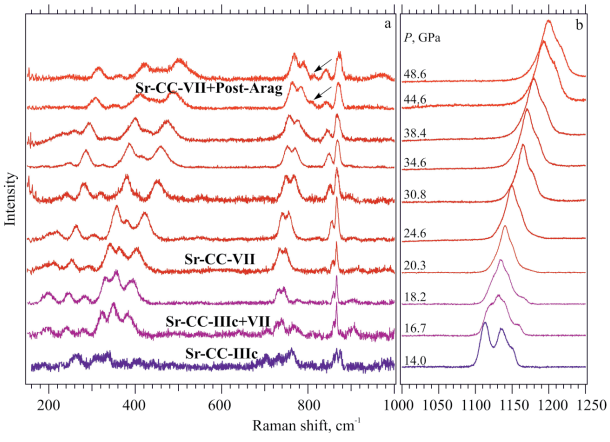

Figure 6. Raman spectra collected at 14–50 GPa (see runs 3 and 4 in Online Materials[1] Fig. OM1) showing formation of Sr-calcite-VII (Sr-CC-VII) and Sr-post-aragonite (Post-Arag) in the room-temperature experiments. The Sr-post-aragonite band appears around 44.6 GPa (marked by arrows). (Color online.)

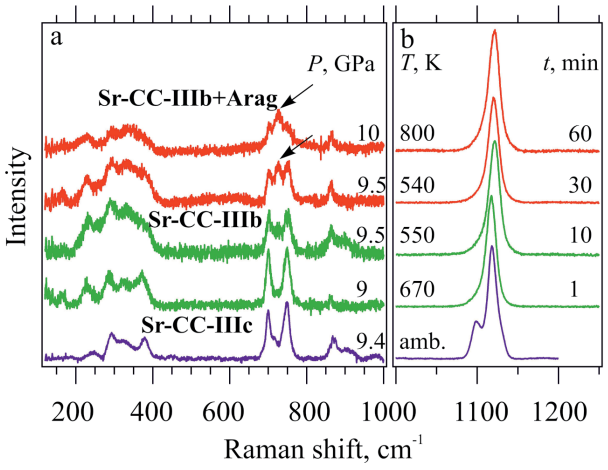

Figure 7. Transformation of Sr-calcite-IIIc (Sr-CC-IIIc) to Sr-calcite-IIIb (Sr-CC-IIIb) and Sr-aragonite (Arag) at high temperature and 9–10 GPa. *P-T* conditions and time from the beginning of heating (*t*) at which spectrum was collected are shown on the figures. The characteristic Sr-aragonite peak is marked by the arrows. (Color online.)

tion with $CaCO_3$-IIIb-like structure will be called Sr-calcite-IIIb. Sr-calcite-IIIb was detected in the pressure range of 1.8–4 GPa (Fig. 1; Online Materials[1] Fig. OM1).

Increase of pressure above 4 GPa leads to a clear and abrupt splitting of the 1100 cm^{-1} band in the Raman spectra (Fig. 5; Online Materials[1] Figs. OM7 and OM8a). Previous studies on the $CaCO_3$ system attributed this splitting to the formation of $CaCO_3$-III (Pippinger et al. 2014; Koch-Müller et al. 2016; Bayarjargal et al. 2018). Consequently, we conclude that Sr-calcite-III has appeared above 4 GPa. This phase was detected in a relatively narrow pres-sure range from 4 to 7 GPa (Fig. 1; Online Materials[1] Fig. OM1).

Another clear change in the Raman spectra takes place above 7 GPa (Fig. 5; Online Materials[1] Figs. OM7–OM9). Even though the spectra above 7 GPa contain a similar set of modes as that of Sr-calcite-III, the bands above 1090 cm^{-1} broaden and shift abruptly to higher wavenumbers (Fig. 5; Online Materials[1] Fig. OM7). The observed changes indicate the appearance of another structural modification. However, the Raman spectra cannot be explained by any known high-pressure polymorphs of $CaCO_3$ (Koch-Müller et al. 2016; Bayarjargal et al. 2018). Based on the similarities in the Raman spectra (Fig. 5; Online Materials[1] Figs. OM7–OM9), we assume that this new high-pressure modification has a closely related structure to that of Sr-calcite-III. Hence, we will refer to it as Sr-calcite-IIIc.

Sr-calcite-IIIc was detected as the only phase in the Raman spectra at room temperature from 7 to 14 GPa (Fig. 6). Further compression of Sr-calcite-IIIc leads to the formation of another high-pressure polymorph between 14–18 GPa (Fig. 6). The transition is sluggish and the sample transforms fully to the high-pressure phase at 20 GPa (Fig. 6). The Raman spectra collected at 20 GPa contain 13 intense bands in the range of 150–1250 cm^{-1} (Fig. 6; Online Materials[1] Figs. OM10 and OM11). The external vibrational modes located below 500 cm^{-1} include at least 7 bands (Fig. 6; Online Materials[1] Fig. OM11). The internal vibrational modes are represented by a single band at 1145 cm^{-1} (v_1) with a shoulder on the high-frequency side, and two doublets at 733, 745 cm^{-1} (v_4), and 862, 868 cm^{-1} (v_2) (Fig. 6; Online Materials[1] Figs. OM10 and OM11).

In pure $CaCO_3$ all previous studies showed the formation of $CaCO_3$-VI above 16 GPa at room temperature (Koch-Müller et al. 2016; Bayarjargal et al. 2018). However, the Raman spectra of the $Ca_{0.82}Sr_{0.18}CO_3$ solid solution show major differences from those of $CaCO_3$-VI (Online Materials[1] Fig. OM12). Raman spectra of $CaCO_3$-VI contain a single v_2 band (850 cm^{-1} at 20 GPa) (Bayar-jargal et al. 2018), while the appearance of the two distinct bands at 850–890 cm^{-1}, as observed in the present study, was reported as the main feature of the $CaCO_3$-VI to -VII transition (Bayarjargal et al. 2018) (Online Materials[1] Fig. OM12). Based on our observa-tions, we conclude that in the $Ca_{0.82}Sr_{0.18}CO_3$ solid solution, we observe the formation of a polymorph with a structure similar to $CaCO_3$-VII (Sr-calcite-VII).

The Raman spectra of $Ca_{0.82}Sr_{0.18}CO_3$ solid solution measured between 20–55 GPa showed the persistence of Sr-calcite-VII up to the highest experimental pressure (Figs. 1 and 6; Online Ma-terials[1] Fig. OM1). A new feature arising at 810 cm^{-1} at 44.6 GPa (Fig. 6; Online Materials[1] Fig. OM10) may indicate the onset of a transition to a post-aragonite phase (Sr-post-aragonite further below) (Bayarjargal et al. 2018). Sr-calcite-VII and Sr-post-aragonite coexist between 44.6–55 GPa at room temperature (Fig. 6; Online Materials[1] Fig. OM10). Formation of both phases at ambient temperature contrasts previous data on pure $CaCO_3$, where the respective polymorphs were detected only after heating (Gavryushkin et al. 2017; Bayarjargal et al. 2018).

In the experimental runs 1 and 2 (Fig. Online Materials[1] Fig. OM1), Raman spectra were also measured on decompression. The decompression of Sr-calcite-VII led to the formation of Sr-calcite-IIIc together with Sr-calcite-IIIb below 16 GPa (Online Materials[1] Figs. OM1, OM8b, and OM8c). Thus,Sr-calcite-IIIb could be observed in two pressure ranges from 1.8 to 4 GPa, and from 7 to 14 GPa (Online Materials[1] Fig. OM1), same as reported by Koch-Müller et al. (2016) for the $CaCO_3$-IIIb. However, the "pressure stability window" of Sr-calcite-IIIb depends on the experimental path.

For better understanding of the Sr-calcite-IIIc and -IIIb behavior, additional high-temperature Raman experiments were carried out at 9–10 GPa and 540–800 K (Fig. 1). First, pressure was increased to 9.4 GPa and Raman spectra were measured before heating (Fig. 7; Online Materials[1] Fig. OM13). Sr-calcite-IIIc was detected at room temperature, confirming the previous observa-tions. After <1 min of heating, Sr-calcite-IIIc fully transformed to Sr-calcite-IIIb (Fig. 7; Online Materials[1] Fig. OM13). Further heating led to the formation of an aragonite-type polymorph (Sr-aragonite) already at 540 K and 9 GPa (Fig. 7; Online Materials[1] Fig. OM13). Sr-aragonite is quenchable to atmospheric pressure and was detected in the Raman spectra collected after experiments (Online Materials[1] Fig. OM13).

Discussion

In this paper, we present the results of the first in situ experimental study on the $CaCO_3$-$SrCO_3$ system, at pressures up to 55 GPa (Fig. 1; Online Materials[1] Fig. OM1). The results of the present study show that incorporation of Sr^{2+} in $CaCO_3$ has a significant effect on the phase behavior of calcium carbonate at high pressures both at room and at high temperature. Below

we discuss the findings of this work in detail, as well as their implications for understanding the structural behavior of carbonates at mantle conditions.

The first synthesis experiment was performed at 2 GPa and 1273 K (1000 °C) (Fig. 1), which according to the $CaCO_3$ phase diagram, corresponds to the $CaCO_3$-IV stability field, close to the calcite-aragonite transition curve (~2.5 GPa, 1273 K) (Ter Heege and Renner 2007). The choice of the *P-T* synthesis parameters was influenced by the fact that a miscibility gap exists in the $CaCO_3$-$SrCO_3$ system at low pressures (Chang and Brice 1972; Carlson 1980). Due to the difference in the ionic radii of Ca^{2+} (1.00 Å) and Sr^{2+} (1.18 Å) (Shannon 1976), miscibility of Sr^{2+} in the calcite structure is limited to 15 mol% at room temperature (Chang and Brice 1972; Carlson 1980; Matsunuma et al. 2014) and ~40 mol% at 973 K (700 °C) (Chang and Brice 1972; Carlson 1980). The coexisting phases in the miscibility gap have orthorhombic aragonite-type and rhombohedral calcite-type structures on the Sr-rich and Ca-rich sides, respectively (Chang and Brice 1972; Carlson 1980). The two-phase field exists up to the transition to the $CaCO_3$-IV anion-disordered phase (*R*3*m*, disordered calcite structure) at 973–1173 K (700–900 °C) (Chang and Brice 1972; Carlson 1980).

In this study we were able to synthesize a $Ca_{0.82}Sr_{0.18}CO_3$ solid solution at 2 GPa and 1273 K (1000 °C). The results of TEM (Fig. 2; Online Materials[1] Fig. OM3) and EDS (Online Materials[1] Fig. OM2) studies show textural and compositional homogeneity of the solid solution. The minor Sr-rich secondary phase was detected as small inclusions along the dislocations and cracks, which allows us to conclude that it is likely a relic of the growth media.

According to the XRD results, $Ca_{0.82}Sr_{0.18}CO_3$ is monoclinic at 2 GPa (Sr-calcite-II, space group $P2_1/c$). MIR- and Raman spectroscopy results show that Sr-calcite-II has a structure similar to that of $CaCO_3$-II, which has been described as a monoclinic distortion of the calcite structure. $CaCO_3$-II is a metastable phase that crystallizes in a narrow pressure range between 1.7 and 2.5 GPa (Pippinger et al. 2014). The majority of the experimental studies show that it is not quenchable to atmospheric pressure and transforms to aragonite upon heating (Merrill and Bassett 1975; Pippinger et al. 2014; Koch-Müller et al. 2016; Bayarjar-gal et al. 2018). However, based on our observations, we can conclude that incorporation of Sr^{2+} in the solid solution expands the stability field of the $CaCO_3$-II-like structure (Sr-calcite-II) to higher temperatures and lower pressures. Moreover, Sr-calcite-II is quenchable to ambient conditions.

As for the effect of cold compression, Sr-calcite-II was observed at room temperature up to 1.8 GPa. Further increase of pressure led to the formation of the following phases: (1) Sr-calcite-IIIb at 1.8–4 GPa; (2) Sr-calcite-III at 4–7 GPa;(3) Sr-calcite-IIIc and/or IIIb at 7–16 GPa; (4) Sr-calcite-VII 16–55 GPa; and (5) Sr-post-aragonite above 45 GPa (Fig. 1; Online Materials[1] Fig. OM1).

The Raman spectra of the Sr-calcite-IIIb, -III, and -IIIc share a lot of similarities (Online Materials[1] Figs. OM8 and OM9), and differ mostly in the symmetric stretching vibration regions (900–1200 cm^{-1}), composed of a single band with a shoulder for the Sr-calcite-IIIb modification, and doublets for the Sr-calcite-III and -IIIc (Online Materials[1] Figs. OM8 and OM9). Comparison of our spectroscopic results with previous publications (Koch-Müller et al. 2016; Bayarjargal et al. 2018) shows that all phases have structures closely related to $CaCO_3$-III and -IIIb. Moreover, the formation of Sr-calcite-IIIb and -III phases in the solid solution occurs at the same *P-T* conditions where the respective $CaCO_3$ polymorphs, $CaCO_3$-IIIb and -III also appear (Fig. 1; Online Materials[1] Fig. OM1) (Pippinger et al. 2014; Koch-Müller et al. 2016; Bayarjargal et al. 2018). The third phase, Sr-calcite-IIIc, is a unique modification, not observed in $CaCO_3$.

$CaCO_3$-IIIb and -III structures are topologically similar and contain non-co-planar CO_3^{2-} groups and two non-equivalent Ca coordination polyhedra ($Ca^{[7]}$ and $Ca^{[9]}$) (Merlini et al. 2012). The main difference between them is in the arrangement of the structural blocks, which results in 10 ($CaCO_3$-III) and 4 ($CaCO_3$-IIIb) formula units, respectively, in the primitive unit cell (Mer-lini et al. 2012). According to DFT calculations, the increased number of atoms in the unit cell of $CaCO_3$-III as compared to $CaCO_3$-IIIb results in the splitting of the v_1, v_2, and v_4 bands in the $CaCO_3$-III spectra (Koch-Müller et al. 2016). Taking into account the previous results on $CaCO_3$-III and -IIIb, and the similarities of the Raman spectra of Sr-calcite-IIIb, -III, and -IIIc, we could speculate that those high-pressure modifications have as well topologically similar structures (Koch-Müller et al. 2016; Bayarjargal et al. 2018). However, as the Raman spectroscopy does not give definite structural solutions, further single-crystal XRD studies are necessary.

The similarity of Sr-calcite-IIIb and -IIIc structures could explain the observed behavior of those phases at high pressure and temperature. Formation of Sr-calcite-IIIc or/and reappearance of Sr-calcite-IIIb occurs between 7 and 16 GPa and depends on the experimental *P-T* path (Fig. 1; Online Materials[1] Fig. OM1). Sr-calcite-IIIc forms in the cold compression experiments, while heating transforms it to Sr-calcite-IIIb. In the decompression experiments at room temperature, Sr-calcite-IIIc and IIIb coexist in the 7–16 GPa pressure range (Online Materials[1] Fig. OM1).

The observed dependence of the phase behavior on the experimental *P-T* path may result from the sensitivity of the Sr-calcite-IIIb and -IIIc formation to the influence of the hydrostatic conditions. Both pressure media, Ar and NaCl, used in this study are non-hydrostatic at high pressure and room temperature (Klotz et al. 2009). Non-hydrostaticity may lead to the stress-induced phase transition at 7 GPa from Sr-calcite-III to -IIIc. On the contrary, thermal annealing and/or pressure decrease can reduce the stress gradient (Angel et al. 2007) and promote formation of the Sr-calcite-IIIb polymorph at similar pressures. Sr-calcite-IIIb under the quasi-hydrostatic conditions forms in two pressure ranges 1.8–4 and 7–16 GPa, showing similar behavior to $CaCO_3$-IIIb (Koch-Müller et al. 2016).

The similar effect of the pressure medium and the experimental *P-T* path on the $CaCO_3$-IIIb formation was previously observed in several experimental studies (i.e., Merlini et al. 2012, 2018; Yuan et al. 2018). In pure $CaCO_3$, non-hydrostaticity suppresses the formation of $CaCO_3$-IIIb and only $CaCO_3$-III could be detected. The addition of Sr^{2+} to the system makes the effect more pronounced and leads to the new structural modification Sr-calcite-IIIc.

Sr-calcite-IIIb and -IIIc are most likely metastable phases in the range of 7–16 GPa. They transform to the aragonite-structured

polymorph, Sr-aragonite, already at 540 K and 9 GPa. The formation of Sr-aragonite is observed at ~200 K lower temperatures than in $CaCO_3$ (Fig. 1).

Another high-pressure polymorph, Sr-calcite-VII appears already at room temperature and at 16 GPa, and it is stable until the highest-pressure point investigated. Above 45 GPa Sr-calcite-VII probably coexists with the Sr-post-aragonite phase. The stability fields of both Sr-calcite-VII and Sr-post-aragonite are located at ~10–15 GPa lower pressures than those of the respective $CaCO_3$ polymorphs (Ono et al. 2005; Gavryushkin et al. 2017; Bayarjargal et al. 2018). Both the formation of Sr-aragonite at much lower temperatures, as well as the appearance of Sr-calcite-VII and Sr-post-aragonite in the cold compression experiments, reveal a significant effect of Sr^{2+} on the kinetics of the pressure-induced structural transformations.

Even though the formation of the $CaCO_3$ polymorphs aragonite, $CaCO_3$-VII, and post-aragonite is thermodynamically favored in the pure $CaCO_3$ system, it is kinetically hindered and occurs in experiments only above 773 K (500 °C) (Fig. 1) (Gavryushkin et al. 2017; Bayarjargal et al. 2018). On cold compression and at low temperatures, $CaCO_3$ transforms to metastable polymorphs, i.e., $CaCO_3$-IIIb instead of aragonite at 7–15 GPa, and $CaCO_3$-VI instead of $CaCO_3$-VII and post-aragonite at 15–50 GPa (Koch-Müller et al. 2016; Bayarjargal et al. 2018).

The introduction of Sr^{2+} to $CaCO_3$ seems to lower the kinetic barrier that prevents the formation of aragonite, $CaCO_3$-VII, and post-aragonite in the end-member $CaCO_3$, and promotes their formation at lower *P-T* conditions. The observed tendency is most likely related to the capacity of the different Ca-carbonate high-pressure polymorphs to accommodate large cations. The known structures of aragonite, $CaCO_3$-VII, and post-aragonite have larger cationic coordination numbers—9, 10, and 12, respectively—than $CaCO_3$-IIIb ($Ca^{[7]}$-$Ca^{[9]}$) and $CaCO_3$-VI ($Ca^{[7+2]}$) (Merlini et al. 2012; Gavryushkin et al. 2017). Ca-carbonate solid solutions with Sr^{2+} favor likely structures with larger coordination sites at lower pressures compared to pure $CaCO_3$.

This tendency is in good agreement with previous observations in both end-members (Wang et al. 2015) and the $CaCO_3$-$SrCO_3$ solid solution (Carlson 1980). Strontianite,$SrCO_3$, tends to form structures with larger coordination numbers at a given pressure, compared to $CaCO_3$: aragonite with $Sr^{[9]}$ at atmospheric pressure, and post-aragonite with $Sr^{[12]}$ already at 20 GPa (Wang et al. 2015). The small amounts of Sr^{2+} in $CaCO_3$ aragonite extend the stability field of aragonite structure to slightly lower pressures than in the unary $CaCO_3$ system (Carlson 1980). The previous high-pressure studies demonstrated the formation of aragonite structured $Ca_{0.80}Sr_{0.20}CO_3$ solid solution at 1.6 GPa and 923 K, which in pure $CaCO_3$ system would still belong to the stability field of calcite (Carlson 1980).

Our experiments show a significant role of the cation in the high-pressure phase transitions of calcium carbonate. The relatively small amount of Sr^{2+} in the synthesized solid solution, 18 mol%, comparable with that found in some diamond inclusions (Logvinova et al. 2008, 2011, 2019a), leads to significant changes in the phase diagram of calcium carbonate: (1) stabilization at high temperatures of the $CaCO_3$-II-type structure (Sr-calcite-II); (2) stress-induced phase transition to the new high-pressure modification, Sr-calcite-IIIc; (3) formation of a polymorph with aragonite type structure at lower temperatures compared with that in $CaCO_3$; and (4) phase transition to Sr-calcite-VII and Sr-post-aragonite already at room temperature and at pressures 10–15 GPa lower than in $CaCO_3$ (Fig. 1; Online Materials[1] Fig. OM1).

The formation of monoclinic Sr-calcite-II at high temperatures raises the important question on whether the metastable $CaCO_3$ polymorphs can become thermodynamically stable in the other calcium carbonate solid solutions as well. For instance, previous studies reported that addition of 5 mol% of Fe^{2+} or Mg^{2+} to $CaCO_3$ stabilizes the calcite structure at 6 GPa and 1273–1473 K (1000–1200 °C) in the *P-T* stability field of $CaCO_3$ aragonite (Shatskiy et al. 2014, 2018; Müller et al. 2017). It is, however, unknown what structures Mg- or Fe-calcites adopt at high pressures and temperatures, as all previous studies examined the samples ex situ (Shatskiy et al. 2014, 2018; Müller et al. 2017).

One of the possibilities, proposed by Merlini et al. (2012), is the stabilization of $CaCO_3$-III-like structures in solid solutions with smaller cations. Due to the different polyhedral site volumes ($Ca^{[7]}$-$Ca^{[9]}$), the structure of $CaCO_3$-III could host cations with different ionic radii without a major elastic strain from non-ideal solid solution. The results of the present study show the fundamental possibility of the stabilization of metastable $CaCO_3$ phases in calcium carbonate solid solutions. Since $CaCO_3$-III transforms back to calcite with the release of pressure, it is necessary to study $CaCO_3$-$MgCO_3$ and $CaCO_3$-$FeCO_3$ in situ at high pressures.

Implications

The present study and previous observations (Shatskiy et al. 2014, 2018; Müller et al. 2017) show that the high-pressure phase behavior of the calcium carbonate-based solid solutions depends strongly on the specific chemical composition of the solid solution. Even substituting a small amount of Ca^{2+} by different cations, such as smaller cations (Mg^{2+} or Fe^{2+}), or bigger ones (Sr^{2+} or Ba^{2+}), shifts phase transition pressures and temperatures and probably also leads to the formation of new crystal structures.

Due to the large coordination sites in aragonite, which is long believed to be the major calcium carbonate polymorph in the upper mantle, the solubility of Mg^{2+} and Fe^{2+} in the structure is limited to few molar percentages (Shatskiy et al. 2014, 2018; Müller et al. 2017), and higher concentrations will promote crys-tallization of phases with smaller cationic sites—either calcite, $CaCO_3$-III, or others that are currently unknown. Indeed, natural aragonites contain only a few molar percentages of $Mg^{2+}$and Fe^{2+}, while there are findings of Mg-rich and Fe-rich calcium carbon-ates with calcite structure in polycrystalline carbonate inclusions in garnets from diamond grade metamorphic rocks (Korsakov et al. 2010; Frezzotti et al. 2011). Thus, we could assume that Mg^{2+} and Fe^{2+} impurities in calcium carbonates will prevent the aragonite formation at the upper mantle conditions down to at least 200 km depth (6 GPa).

On the contrary, the present experimental data shows that structures with large cation sites (aragonite, $CaCO_3$-VII, and post-aragonite) are favorable and will likely be observed only in the pure $CaCO_3$, in carbonates with larger cations such as $SrCO_3$ and $BaCO_3$, and in their solid solutions. Our high-temperature experiments show that syngenetic (Sr,Ca)-carbonate inclusions in diamonds should have aragonite-type structure.

Because of the generally very small size of inclusions (Klein-BenDavid et al. 2006, 2009), which, furthermore, contain multi-phase assemblages of solid phases (silicates, oxides, carbonates), brines (halides), and fluid bubbles, the analytical techniques for the accurate investigation of the structures and compositions of the minerals are largely confined to TEM (Klein-BenDavid et al. 2006, 2009; Logvinova et al. 2008, 2011, 2019a; Kaminsky et al. 2009), IR, and Raman spectroscopy (Logvinova et al. 2008, 2011, 2019a; Kaminsky et al. 2009). Most of the currently available studies on $(Ba,Ca)CO_3$, $(Sr,Ca)CO_3$, and $(Ca,Ba,Sr)CO_3$ used the TEM method and IR spectroscopy and focused on the composition of the minerals rather than the structures (Klein-BenDavid et al. 2006, 2009; Logvinova et al. 2008, 2011, 2019a). However, in the paper by Kaminsky et al. (2009), Sr- and Ba-bearing calcium carbonate (Ca = 99.26 mol%), which was found in the diamond nano-inclusions with the low mantle minerals walstromite-structured $CaSiO_3$, $CaTiO_3$, and ferropericlase, was identified as rhombohedral calcite with the aid of Raman spectroscopy. According to the $CaCO_3$ phase diagram (Bayarjargal et al. 2018), at the low mantle conditions, three carbonate phases could be stable: aragonite, $CaCO_3$-VII, and post-aragonite. Aragonite is quenchable to ambient condi-tions, while post-aragonite and $CaCO_3$-VII transform back to calcite on decompression. Given that the addition of Sr^{2+} and Ba^{2+} stabilizes both $CaCO_3$-VII and post-aragonite type structures at lower pressures, we could assume that the crystallization of the $(Ca,Ba,Sr)CO_3$ in the inclusions should have happened above 20–25 GPa likely in $CaCO_3$-VII or post-aragonite type structures.

Inclusions in natural diamonds provide direct samples of the diamond forming media and could be used to reconstruct the physical-chemical environments in which their host diamonds were formed. $(Ba,Ca)CO_3$, $(Sr,Ca)CO_3$, and $(Ca,Ba,Sr)CO_3$, despite the scarcity of the findings in inclusions of typical kim-berlite and placer diamonds, are vivid indicators of metasomatic processes (Logvinova et al. 2008, 2011, 2019a). They appear in unique polyphase assemblages together with phosphates, halides, sheet silicates, and abundant fluid segregations and indicate the involvement of a carbonatitic high-density fluid/melt enriched in incompatible elements in the diamond formation (Cl, K, P, Ba, and Sr) (Klein-BenDavid et al. 2006, 2009; Logvinova et al. 2008, 2011, 2019a). The carbon isotopic composition of the host diamonds and predominant eclogitic paragenesis of mineral inclusions imply that this fluid/melt might have been supplied from the subducted rocks of the oceanic and continental litho-sphere (Ragozin et al. 2009).

Thus, the carbonate phase diagrams, *P-T* parameters of the phase transitions, and melting temperatures are a useful tool for better understanding of the mantle processes and the recon-struction of their physical-chemical conditions. In particular, $CaCO_3$-$SrCO_3$ and $CaCO_3$-$BaCO_3$ systems are important for the reconstructions of the processes related to the carbonatites metosomatic activity.

The present study shows that the high-pressure phase be-havior of the calcium carbonate-based solid solutions depends strongly on the specific chemical composition of the solid solu-tion. The structural changes derived from the cationic substitution can have an important impact on the phase diagrams of carbon-ates and, thus, affect the physical properties of these materials such as equations of state, sound velocities, melting temperatures, and other factors. They should be considered in the modeling of the processes that involve carbonates. Overall, it is clear that the carbonate phase diagrams in the complex multi-component systems should be further studied with the use of in situ methods.

References

Angel, R.J., Bujak, M., Zhao, J., Gatta, G.D., and Jacobsen, S.D. (2007) Effective hydrostatic limits of pressure media for high-pressure crystallographic studies. Journal of Applied Crystallography, 40, 26-32.

Bayarjargal, L., Fruhner, C.J., Schrodt, N., and Winkler, B. (2018) $CaCO_3$ phase diagram studied with Raman spectroscopy at pressures up to 50 GPa and high temperatures and DFT modeling. Physics of the Earth and Planetary Interiors, 281, 31-45.

Brenker, F.E., Vollmer, C., Vincze, L., Vekemans, B., Szymanski, A., Janssens, K., Szaloki, I., Nasdala, L., Joswig, W., and Kaminsky, F. (2007) Carbonates from the lower part of transition zone or even the lower mantle. Earth and Planetary Science Letters, 260, 1-9.

Carlson, W.D. (1980) The calcite–aragonite equilibrium: effects of Sr substitution and anion orientational disorder. American Mineralogist, 65, 1252-1262.

Chang, L.L., and Brice, W.R. (1972) Subsolidus phase relations in aragonite-type carbonates: II. The systems $CaCO_3$-$SrCO_3$-$PbCO_3$ and $CaCO_3$-$BaCO_3$-$PbCO_3$. American Mineralogist: Journal of Earth and Planetary Materials, 57, 155-168.

Dasgupta, R., and Hirschmann, M.M. (2006) Melting in the Earth's deep upper mantle caused by carbon dioxide. Nature, 440, 659-62.

Datchi, F., Dewaele, A., Loubeyre, P., Letoullec, R., Le Godec, Y., and Canny, B. (2007) Optical pressure sensors for high-pressure–high-temperature studies in a diamond anvil cell. High Pressure Research, 27, 447-463.

Dewaele, A., Torrent, M., Loubeyre, P., and Mezouar, M. (2008) Compression curves of transition metals in the Mbar range: Experiments and projector augmented-wave calculations. Physical Review B, 78, 104102.

Frezzotti, M.L., Selverstone, J., Sharp, Z.D., and Compagnoni, R. (2011) Carbonate dissolution during subduction revealed by diamond-bearing rocks from the Alps. Nature Geoscience, 4, 703-706.

Gavryushkin, P.N., Martirosyan, N.S., Inerbaev, T.M., Popov, Z.I., Rashchenko, S.V., Likhacheva, A.Y., Lobanov, S.S., Goncharov, A.F., Prakapenka, V.B., and Litasov, K.D. (2017) Aragonite-II and $CaCO_3$-VII: New High-Pressure, High-Temperature Polymorphs of $CaCO_3$. Crystal Growth and Design, 17, 6291-6296.

Irving, A.J., and Wyllie, P.J. (1973) Melting relationships in CaO-CO_2 and MgO-CO_2 to 36 kilobars with comments on CO_2 in the mantle. Earth and Planetary Science Letters, 20, 220-225.

Kamenetsky, V.S., and Yaxley, G.M. (2015) Carbonate–silicate liquid immiscibility in the mantle propels kimberlite magma ascent. Geochimica et Cosmochimica Acta, 158, 48-56.

Kaminsky, F., Wirth, R., Matsyuk, S., Schreiber, A., and Thomas, R. (2009) Nyerereite and nahcolite inclusions in diamond: evidence for lower-mantle carbonatitic magmas. Mineralogical Magazine, 73, 797-816.

Kaminsky, F.V., Wirth, R., and Schreiber, A. (2013) Carbonatitic inclusions in deep mantle diamonds from Juina, Brazil: new minerals in the carbonate-halide association. The Canadian Mineralogist, 51, 669-688.

Kiseeva, E.S., Yaxley, G.M., Hermann, J., Litasov, K.D., Rosenthal, A. and Kamenetsky, V.S. (2012). An Experimental Study of Carbonated Eclogite at 3.5-5.5 GPa-Implications for Silicate and Carbonate Metasomatism in the Cratonic Mantle. Journal of Petrology, 53, 727-759.

Kiseeva, E.S., Litasov, K.D., Yaxley, G.M., Ohtani, E. and Kamenetsky, V.S. (2013). Melting and phase relations of carbonated eclogite at 9–21 GPa and the petrogenesis of alkali-rich melts in the deep mantle. Journal of Petrology, 54, 1555-1583.

Klein-BenDavid, O., Wirth, R. and Navon, O. (2006). TEM imaging and analysis of microinclusions in diamonds: A close look at diamond-growing fluids. American Mineralogist, 91, 353-365.

Klein-BenDavid, O., Logvinova, A.M., Schrauder, M., Spetius, Z.V., Weiss, Y., Hauri, E.H., Kaminsky, F.V., Sobolev, N.V. and Navon, O., (2009). High-Mg carbonatitic microinclusions in some Yakutian diamonds – a new type of diamond-forming fluid. Lithos, 112, 648-659.

Klotz, S., Chervin, J.C., Munsch, P., and Le Marchand, G. (2009) Hydrostatic limits of 11 pressure transmitting media. Journal of Physics D: Applied Physics, 42, 075413

Koch-Müller, M., Jahn, S., Birkholz, N., Ritter, E., and Schade, U. (2016) Phase transitions in the system $CaCO_3$ at high *P* and *T* determined by in situ vibrational spectroscopy in diamond anvil cells and first-principles simulations. Physics and Chemistry of Minerals, 43, 545-561.

Korsakov, A.V., De Gussem, K., Zhukov, V.P., Perraki, M., Vandenabeele, P., and Golovin, A.V. (2009) Aragonite-calcite-dolomite relationships in UHPM polycrystalline carbonate inclusions from the Kokchetav Massif, northern Kazakhstan. European Journal of Mineralogy, 21, 1301-1311.

Korsakov, A.V., De Gussem, K., Zhukov, V.P., Perraki, M., Vandenabeele, P., and Golovin, A.V. (2010) Aragonite-calcite-dolomite relationships in UHPM polycrystalline carbonate

inclusions from the Kokchetav Massif, northern Kazakhstan. European Journal of Mineralogy, 21, 1301-1311.

Kuznetsov, A., Semikhatov, M., and Gorokhov, I. (2014) The Sr isotope chemostratigraphy as a tool for solving stratigraphic problems of the Upper Proterozoic (Riphean and Vendian). Stratigraphy and Geological Correlation, 22, 553-575.

Lobanov, S.S., Dong, X., Martirosyan, N.S., Samtsevich, A.I., Stevanovic, V., Gavryushkin, P.N., Litasov, K.D., Greenberg, E., Prakapenka, V.B., Oganov, A.R., and Goncharov, A.F. (2017) Raman spectroscopy and x-ray diffraction of sp^3-$CaCO_3$ at lower mantle pressures. Physical Review B, 96, 104101

Logvinova, A.M., Wirth, R., Fedorova, E.N., and Sobolev, N.V. (2008) Nanometre-sized mineral and fluid inclusions in cloudy Siberian diamonds: new insights on diamond formation. European Journal of Mineralogy, 20, 317-331.

Logvinova, A.M., Wirth, R., Tomilenko, A.A., Afanas'ev, V.P., and Sobolev, N.V. (2011) The phase composition of crystal-fluid nanoinclusions in alluvial diamonds in the northeastern Siberian Platform. Russian Geology and Geophysics, 52, 1286-1297.

Logvinova, A., Zedgenizov, D., and Wirth, R. (2019a) Specific Multiphase Assemblages of Carbonatitic and Al-Rich Silicic Diamond-Forming Fluids/Melts: TEM Observation of Microinclusions in Cuboid Diamonds from the Placers of Northeastern Siberian Craton. Minerals, 9 (1), 50

Logvinova, A.M., Shatskiy, A., Wirth, R., Tomilenko, A.A., Ugap'eva, S.S., and Sobolev, N.V. (2019b) Carbonatite melt in type Ia gem diamond. Lithos, 342, 463-467.

Matsunuma, S., Kagi, H., Komatsu, K., Maruyama, K., and Yoshino, T. (2014) Doping incompatible elements into calcite through amorphous calcium carbonate. Crystal Growth & Design, 14, 5344-5348.

Merlini, M., Hanfland, M., and Crichton, W.A. (2012) $CaCO_3$-III and $CaCO_3$-VI, high-pressure polymorphs of calcite: Possible host structures for carbon in the Earth's mantle. Earth and Planetary Science Letters, 333, 265-271.

Merlini, M., Crichton, W.A., Chantel, J., Guignard, J., and Poli, S. (2018) Evidence of interspersed co-existing $CaCO_3$-III and $CaCO_3$-IIIb structures in polycrystalline $CaCO_3$ at high pressure. Mineralogical Magazine, 78, 225-233.

Merrill, L., and Bassett, W.A. (1975) The crystal structure of $CaCO_3$ (II), a high-pressure metastable phase of calcium carbonate. Acta Crystallographica Section B: Structural Crystallography and Crystal Chemistry, 31, 343-349.

Müller, J., Koch-Müller, M., Rhede, D., Wilke, F.D., and Wirth, R. (2017) Melting relations in the system $CaCO_3$-$MgCO_3$ at 6 GPa. American Mineralogist, 102, 2440-2449.

Ono, S., Kikegawa, T., Ohishi, Y., and Tsuchiya, J., (2005) Post-aragonite phase transformation in $CaCO_3$ at 40 GPa. American Mineralogist, 90, 667-671.

Ono, S., Kikegawa, T., and Ohishi, Y. (2007) High-pressure transition of $CaCO_3$. American Mineralogist, 92, 1246-1249.

Palyanov, Y.N., Sokol, A., Borzdov, Y.M., Khokhryakov, A., and Sobolev, N. (1999) Diamond formation from mantle carbonate fluids. Nature, 400, 417-418.

Pippinger, T., Miletich, R., Merlini, M., Lotti, P., Schouwink, P., Yagi, T., Crichton, W.A., and Hanfland, M. (2014) Puzzling calcite-III dimorphism: crystallography, high-pressure

behavior, and pathway of single-crystal transitions. Physics and Chemistry of Minerals, 42, 29-43.

Ragozin, A., Shatskii, V. anf Zedgenizov, D. (2009). New data on the growth environment of diamonds of the variety V from placers of the northeastern Siberian platform. Doklady Earth Sciences, 425 (2), 436.

Romanenko, A.V., Rashchenko, S.V., Kurnosov, A., Dubrovinsky, L., Goryainov, S.V., Likhacheva, A.Y. and Litasov, K.D. (2018) Single-standard method for simultaneous pressure and temperature estimation using Sm^{2+}:SrB_4O_7 fluorescence. Journal of Applied Physics, 124, 165902.

Scheetz, B., and White, W. (1977) Vibrational spectra of the alkaline earth double carbonates. American Mineralogist, 62, 36-50.

Shannon, R.D. (1976). Revised effective ionic radii and systematic studies of interatomic distances in halides and chalcogenides. Acta crystallographica section A: crystal physics, diffraction, theoretical and general crystallography, 32, 751-767.

Sharygin, I.S., Litasov, K.D., Shatskiy, A., Golovin, A.V., Ohtani, E., and Pokhilenko, N.P. (2015) Melting phase relations of the Udachnaya-East Group-I kimberlite at 3.0–6.5 GPa: Experimental evidence for alkali-carbonatite composition of primary kimberlite melts and implications for mantle plumes. Gondwana Research, 28, 1391-1414.

Shatskiy, A., Borzdov, Y.M., Litasov, K.D., Kupriyanov, I.N., Ohtani, E., and Palyanov, Y.N. (2014) Phase relations in the system $FeCO_3$-$CaCO_3$ at 6 GPa and 900-1700 C and its relation to the system $CaCO_3$-$FeCO_3$-$MgCO_3$. American Mineralogist, 99, 773-785.

Shatskiy, A., Podborodnikov, I.V., Arefiev, A.V., Minin, D.A., Chanyshev, A.D., and Litasov, K.D. (2018) Revision of the $CaCO_3$–$MgCO_3$ phase diagram at 3 and 6 GPa. American Mineralogist, 103, 441-452.

Stachel, T., and Harris, J. (2008) The origin of cratonic diamonds – constraints from mineral inclusions. Ore Geology Reviews, 34, 5-32.

Stachel, T., Harris, J.W., Brey, G.P., and Joswig, W. (2000) Kankan diamonds (Guinea) II: lower mantle inclusion parageneses. Contributions to Mineralogy and Petrology, 140, 16-27.

Suito, K., Namba, J., Horikawa, T., Taniguchi, Y., Sakurai, N., Kobayashi, M., Onodera, A., Shimomura, O., and Kikegawa, T. (2001) Phase relations of $CaCO_3$ at high pressure and high temperature. American Mineralogist, 86, 997-1002.

Ter Heege, J.H., and Renner, J. (2007) In situ impedance spectroscopy on pyrophyllite and $CaCO_3$ at high pressure and temperature: phase transformations and kinetics of atomistic transport. Physics and Chemistry of Minerals, 34, 445-465.

Vahur, S., Teearu, A., Peets, P., Joosu, L., and Leito, I. (2016) ATR-FT-IR spectral collection of conservation materials in the extended region of 4000–80 cm^{-1}. Analytical and Bioanalytical Chemistry, 408, 3373-3379.

Walker, D., Carpenter, M., and Hitch, C. (1990) Some simplifications to multianvil devices for high pressure experiments. American Mineralogist, 75, 1020-1028.

Wang, M., Liu, Q., Nie, S., Li, B., Wu, Y., Gao, J., Wei, X., and Wu, X. (2015) High-pressure phase transitions and compressibilities of aragonite-structure carbonates: $SrCO_3$ and $BaCO_3$. Physics and Chemistry of Minerals, 42, 517-527.

White, W.B. (1974) The carbonate minerals. In V.C. Farmer, Ed., The Infrared Spectra of the Minerals, p. 227–284. Monograph, Mineralogical Society, London.

Wirth, R. (2009) Focused Ion Beam (FIB) combined with SEM and TEM: Ad-vanced analytical tools for studies of chemical composition, microstructure and crystal structure in geomaterials on a nanometre scale. Chemical Geology, 261, 217–229.

Wojdyr, M. (2010) Fityk: a general-purpose peak fitting program. Journal of Applied Crystallography, 43, 1126–1128.

Yaxley, G.M., Crawford, A.J., and Green, D.H. (1991) Evidence for carbonatite metasomatism in spinel peridotite xenoliths from western Victoria, Australia. Earth and Planetary Science Letters, 107, 305-317.

Yuan, X., Gao, C., and Gao, J. (2018) An in situ study of the phase transitions among $CaCO_3$ high-pressure polymorphs. Mineralogical Magazine, 83, 191-197.